An alpaca nanobody neutralizes SARS-CoV-2 by blocking receptor interaction

Leo Hanke[1], Laura Vidakovics Perez[1], Daniel J Sheward[1,4], Hrishikesh Das[2], Tim Schulte[3], Ainhoa Moliner Morro[1], Martin Corcoran[1], Adnane Achour[3], Gunilla Karlsson Hedestam[1], B. Martin Hällberg[2], Ben Murrell[1*] and Gerald M McInerney[1*]

[1]Department of Microbiology, Tumor and Cell Biology, [2]Department of Cell and Molecular Biology and [3]Science for Life Laboratory, Department of Medicine Solna, Karolinska Institutet, and Division of Infectious Diseases, Karolinska University Hospital, Solna, Stockholm, Sweden. [4]Division of Virology, Institute of Infectious Diseases and Molecular Medicine, Faculty of Health Sciences, University of Cape Town, South Africa.

* These authors contributed equally.

For correspondence: Ben Murrell (benjamin.murrell@ki.se), Martin Hällberg (martin.hallberg@ki.se) and Gerald McInerney (gerald.mcinerney@ki.se).

Abstract

We report the isolation and characterization of an alpaca-derived, single domain antibody fragment (nanobody) that specifically targets the receptor binding domain (RBD) of the SARS-CoV-2 spike glycoprotein (spike) and potently neutralizes the virus. A cryo-electron microscopy structure of the bound complex at 2.9 Å resolution reveals that the nanobody (Ty1) binds to an epitope on the RBD accessible in both the 'up' and 'down' conformations and that Ty1 sterically hinders RBD-ACE2 binding. Mechanistic characterization confirms that Ty1 directly interferes with host cell receptor binding. This 12.8 kDa nanobody binds the SARS-CoV-2 spike with high specificity and affinity, and can be produced in high quantities recombinantly thereby offering potential as a potent and widely accessible SARS-CoV-2 antiviral agent.

Introduction

SARS-CoV-2 emerged as the etiologic agent of covid-19 in Wuhan, China in late 2019. In the comparatively short time since then, it has achieved pandemic status, causing more than 5.5 million cases, leading to at least 378,000 deaths and rising. Accordingly, the WHO declared the pandemic to be a public health emergency of international concern. A safe and effective vaccine is urgently needed, but requires time to develop. In the meantime, and indeed also in the post-vaccine era, highly specific and potent antiviral interventions are needed. Many generic or repurposed candidates are in trials, but so far results have been unremarkable. Since the virus is newly emerged, specifically designed drugs have not yet reached late phase trials. When available, specific antiviral drugs or antibody therapies will be used to protect individuals at risk and their widespread use will allow immunologically naïve populations to exit lockdowns more safely.

52 The virus is closely related to SARS-CoV-1, both being members of the lineage 2
53 betacoronaviruses. Cell entry of both viruses is achieved by first binding to the cell surface
54 expressed receptor angiotensin-converting enzyme 2 (ACE2), followed by conformational
55 changes in the viral spike glycoprotein trimer and subsequent membrane fusion. The affinity of
56 SARS-CoV-2 receptor binding domain (RBD) for ACE2 is considerably higher than that for
57 SARS-CoV-1 [1,2], supporting efficient cell entry and likely contributing to pathogenesis. The
58 RBD is a globular domain situated on the distal surface of the spike protein. Two conformations
59 have been observed in the stabilized trimer. Specifically, one conformation where one RBD is
60 ACE2-accessible while two are not and one conformation where all three RBDs are down, i.e.
61 receptor inaccessible [2,3]. As the receptor-engaging part of the spike, the RBD is an attractive
62 target for coronavirus neutralization, and a number of conventional neutralizing monoclonal
63 antibodies that target the RBD and block receptor binding have already been isolated from
64 convalescent patients [4–6].
65
66 Camelid-derived single domain antibody fragments, also called VHHs or nanobodies, offer
67 several advantages over conventional antibodies as candidates for specific therapies. Despite
68 being approximately one tenth of the size of a conventional antibody, they retain specificity and
69 affinity similar to conventional antibodies while being far easier to clone, express and
70 manipulate. They are readily expressed in bacteria in large quantities and show high thermal
71 stability and solubility, making them easily scalable and extremely cost effective. Their
72 modularity means that they can be oligomerized to increase avidity or to increase serum half-life
73 [7]. Critical to their use as antivirals in humans, they can easily be humanized with existing
74 protocols [8]. Importantly, they have proven to be highly potent inhibitors of viral infections in
75 vivo, particularly respiratory infections [9,10].
76

77 Here, we describe the isolation, evaluation and molecular determination of an alpaca-derived
78 nanobody, Ty1, directed to the receptor-binding domain of the SARS-CoV-2 spike glycoprotein.
79 We demonstrate that the monomeric 12.8 kDa Ty1 molecule potently neutralizes SARS-CoV-2
80 spike pseudovirus. The nanobody binds with high affinity to the RBD in a manner that occludes
81 ACE2 interaction. We have also determined the mechanism of neutralization to be due to direct
82 interference with RBD binding to ACE2. Altogether, these results highlight the great potential of
83 Ty1 as a SARS-CoV-2 antiviral agent.
84
85 **Results**
86
87 Generation of SARS-CoV-2 RBD-specific nanobodies
88
89 We immunized one alpaca with SARS-CoV-2 S1-Fc and RBD in a 60-day immunization
90 schedule. We generated a phage display library and performed two consecutive rounds of
91 phage display, followed by an ELISA-based binding screen (Fig. 1A). We isolated one
92 nanobody, Ty1, that binds specifically to the RBD of the SARS-CoV-2 spike glycoprotein. In
93 parallel we performed next generation sequencing (NGS) on the baseline and post-enrichment
94 libraries, and quantified variant frequency before and after each enrichment step. Ty1 exhibited
95 the greatest fold-change in frequency among all nanobody variants, increasing over 10,000-fold
96 from baseline to after the second enrichment round (Fig.1B). We report the amino acid
97 sequence of Ty1 in Figure 1C.

98 Ty1 neutralizes SARS-CoV-2 spike pseudotyped viruses
99
100 To determine whether Ty1 neutralized SARS-CoV-2 we employed an *in vitro* neutralization
101 assay using lentiviral particles pseudotyped with the SARS-CoV-2 spike protein. Ty1 neutralized

102 SARS-CoV-2 pseudotyped viruses at an IC_{50} of 0.77 µg/ml (54 nM) (Fig. 2A). No neutralization
103 of a lentivirus pseudotyped with VSV-G by Ty1 was evident, and control nanobodies produced
104 and purified in the same way, but specific for either influenza A virus nucleoprotein [11] or GFP
105 [12], showed no evidence of neutralization of SARS-CoV-2 pseudotyped viruses.
106
107 Ty1 specifically recognizes the SARS-CoV-2 spike protein in transfected and infected cells
108
109 To confirm that Ty1 is directed against the SARS-CoV-2 spike protein, we characterized the
110 specificity of Ty1 by flow cytometry. We site-specifically conjugated a fluorophore to the C-
111 terminus of the Ty1 by means of a Sortase A reaction and copper-free click chemistry (Ty1-
112 AS635P), and stained untransfected cells and cells transiently transfected with SARS-CoV-2
113 spike under permeabilizing conditions (Fig. 2B). While untransfected and unstained cells
114 displayed similar signals, cells expressing the viral spike protein showed a strong shift in
115 fluorescence intensity when stained with Ty1-AS635P. The apparent double peak likely
116 reflected the varying efficiency of this transient transfection. To determine if the same probe can
117 be exploited to recognize the viral spike protein in immunofluorescence, we infected Vero E6
118 cells with infectious SARS-CoV-2 at MOI 1 for 24 hours and stained the fixed and permeabilized
119 cells with Ty1-AS635P and anti-dsRNA antibody (Fig. 2C). While uninfected cells showed no
120 signal, infected cells were strongly labelled with both dsRNA antibody and Ty1-AS635P. Thus,
121 Ty1 recognized the viral spike glycoprotein with high specificity in its native conformation in
122 SARS-CoV-2-infected cells. Importantly, the low background in both experiments also
123 suggested that Ty1 is a highly specific and suitable tool for research, diagnostics and therapy.
124
125
126

127 Ty1 competes directly with ACE2 for binding to the RBD of SARS-CoV-2 spike

128 To understand the neutralizing activity, we evaluated the effect of Ty1 on RBD binding to ACE2.
129 We site-specifically conjugated a fluorophore to the C-terminus of the RBD (RBD-AS635P) and
130 used this probe to stain ACE2 expressing HEK293T cells (Fig. 2D). Preincubation of RBD-
131 AS635P with unlabeled Ty1 resulted in a significant reduction of ACE2 staining, while
132 preincubation with the control nanobody NP-VHH1 had no such effect. This result indicated that
133 Ty1 directly prevents binding of SARS-CoV-2 RBD to its host cell receptor ACE2.

134 Ty1 binds the RBD with high affinity

135

136 The highly specific and high-affinity binding of Ty1 to the RBD was also confirmed in kinetic bio
137 layer interferometry (BLI) experiments. Monomeric RBD bound to surface-immobilized Ty1, but
138 not to NP-VHH1 or to biocytin-quenched Streptavidin (SAX) (Fig. 3A). Dipping of the two Ty1-
139 sensors into RBD at a concentration of 550 nM yielded binding responses with fast association
140 kinetics and amplitudes reaching 1.5 nm (red curves), while dipping of the two NP-VHH1-
141 sensors into the same RBD solutions yielded responses comparable to the reference sensors
142 (2x violet and blue as well as light-green curves, respectively). RBD did not bind to the SAX
143 control (green curves). Approximately half of RBD remained bound to Ty1 after 45 min (2700 s)
144 of dissociation.
145 Titration experiments performed under normal and high salt conditions revealed concentration-
146 dependent kinetic response curves for binding of RBD to Ty1 (Fig. 3B). The derived semi-log
147 concentration-response curves revealed sigmoidal line-shapes with fitted apparent K_D-values of
148 8 ± 1.5 and 13 ± 1.5 nm for binding at normal and high salt conditions, respectively.
149 Kinetic fits of each sensorgram applying a 1:1 binding model revealed reasonable fits for
150 association phases of curves obtained at low and intermediate RBD concentrations, as well as
151 for most dissociation curves (Fig. 3B and 3C, left panels). However, relatively large deviations of

152 the fits showed that the 1:1 interaction model did not fully explain the obtained data (residuals in
153 Fig. 3C). Nevertheless, most of the single-sensorgram fits yielded K_D-values in the 10-100 nM
154 range with association and dissociation constants of about 1-1.2 $*10^5$ $(Ms)^{-1}$ and 3.5–4.3$*10^{-3}$ s^{-1}
155 (k_{on} versus K_D plot in the lower panel of Fig. 3B). Most protein-protein interactions have
156 association rates in the 10^6 to 10^7 $M^{-1}s^{-1}$ range, therefore high-affinity interactions with K_D-
157 values in the nM range have typically dissociation rates around $1*10^{-3}$ s^{-1} [13].
158 Altogether, we concluded from these results that RBD bound to surface-immobilized Ty1 with
159 high affinity in the 5-50 nM range.
160
161 Cryo-EM of prefusion spike in complex with Ty1
162
163 To understand the structural basis underlying the potent neutralization of SARS-CoV-2 we
164 performed a preliminary cryo-EM structure determination of the prefusion-stabilized spike
165 ectodomain in complex with Ty1. The current cryo-EM reconstruction reaches an overall
166 resolution of 2.9 Å (Fig. 4A; 0.143 FSC) with strong variation of estimated local resolution from
167 high resolution in the core of the spike trimer to relatively low resolution in the top of the spike.
168 Nevertheless, the current reconstruction clearly shows that the spike retains only one main
169 conformation with one RBD 'up' and two RBDs 'down'. Importantly, all three RBDs are
170 decorated in their upper parts with a Ty1 nanobody. The nanobodies retain a similar binding
171 orientation to the RBD whether the RBD is found in the 'up' or 'down' conformation (Fig. 4B,C).
172 As ACE2 can only be bound by an RBD in the 'up' conformation, the current cryo-EM
173 reconstruction clearly shows that ACE2 binding is sterically hindered from two sides (Fig. 4D).
174 Specifically, ACE2 binding is blocked both by the Ty1 nanobody bound to the RBD in the 'up'
175 conformation and the neighboring RBD in the 'down' conformation. Hence, ACE2 binding is
176 sufficiently hindered with any two of the available three binding RBD sites in the spike trimer. As

177 the RBD-Ty1 interaction interface is poorly resolved in the present reconstruction, we currently
178 refrain from molecular modelling of the exact binding interactions.
179
180 **Discussion**
181
182 The current coronavirus pandemic has drastic consequences for the world's population, and
183 vaccines, antibodies or antivirals are urgently needed. Neutralizing antibodies can block virus
184 entry at an early step of infection and potentially protect individuals that are at high risk of
185 developing severe disease. We report the identification and characterization of a SARS-CoV-2
186 RBD-specific single domain antibody fragment (nanobody) termed Ty1 that potently neutralizes
187 the virus. We provide structural and mechanistic insights that demonstrate that Ty1 prevents
188 RBD binding to its host cell receptor ACE2, and thus prevents SARS-CoV-2 virions from
189 attaching to cells. Ty1 binds the RBD with a kD within the 5-50 nM range, and neutralizes
190 SARS-CoV-2 pseudotyped virus at an $IC_{50}$of 0.77ug/ml (54 nM), representing the most potent
191 SARS-CoV-2 specific nanobody reported to date.
192 We identified Ty1 by binding assay after consecutive rounds of phage display, simultaneously
193 monitoring sequence enrichment by NGS. Although Ty1 exhibited the greatest fold-enrichment
194 in the NGS analysis, multiple additional nanobodies exhibited enrichment of varying extent
195 across both rounds. As the correlation between phage display enrichment and neutralization is
196 likely imperfect, further analyses of our libraries will likely yield other potent SARS-CoV-2
197 neutralizing nanobodies. In addition to neutralization activity, we also show that Ty1 can be
198 used as a detection reagent in flow cytometry and immunofluorescence demonstrating its
199 suitability as a research tool and for diagnostics.
200 It should be noted that the nanobody Ty1 can be readily produced in bacteria at very high yield
201 (in excess of 30 mg/L culture), and shows high affinity, making it an excellent candidate as a
202 low-cost, scalable antiviral agent against SARS-CoV-2, and we provide the amino acid

203 sequence, encouraging direct exploitation as such. While a llama nanobody capable of binding
204 SARS-CoV-2 has recently been isolated, this molecule was elicited against SARS-CoV-1 and
205 Fc-fusion was required to mediate neutralization of SARS-CoV-2 [14], precluding expression in
206 bacterial culture. Since Ty1 already neutralizes as a monomeric protein, the generation of
207 homodimeric or trimeric fusion constructs is likely to further increase its neutralization activity.
208 Our structural results provide a template for the rational design of such oligomers that will
209 potentially 'lock' the spike in a receptor-inaccessible conformation. Based on our work, we hope
210 that Ty1 can be investigated as a candidate for antiviral therapy.
211

212 **Methods**

213 **Cells and virus**

214 Vero E6 cells and HEK293T cells (ATCC-CRL-3216) were maintained in Dulbecco's Modified
215 Eagle Medium (Gibco) supplemented with 10% fetal calf serum and 1% Penicillin-Streptomycin
216 and cultured at 37°C in a humidified incubator with 5% CO_2. A HEK293T cell line engineered to
217 overexpress human ACE2 (HEK293T-ACE2) was generated by the lentiviral transduction of
218 HEK293T cells. Briefly, lentiviruses were produced by co-transfecting HEK293T cells with a
219 plasmid encoding VSV-G (Addgene cat#12259), a lentiviral Gag-Pol packaging plasmid
220 (Addgene cat#8455), and a human ACE2 transfer plasmid. Virions were harvested from the
221 supernatant, filtered through 0.45 µm filters, and used to transduce HEK293T cells. All cell lines
222 used for experiments were negative for *Mycoplasma* as determined by PCR.
223

224 Infectious SARS-CoV-2 [15] was propagated in Vero E6 cells and titrated by plaque assay.

225 **Proteins and probes.**

226 The plasmid for expression of the SARS-CoV-2 prefusion-stabilized spike ectodomain with a C-
227 terminal T4 fibritin trimerization motif was obtained from [2]. The plasmid was used to transiently

228 transfect FreeStyle 293F cells using FreeStyle MAX reagent (Thermo Fisher Scientific). The S
229 ectodomain was purified from filtered supernatant on Streptactin XT resin (IBA Lifesciences),
230 followed by size-exclusion chromatography on a Superdex 200 in 5 mM Tris pH 8, 200 mM
231 NaCl.

232 The RBD domain (RVQ – VNF) of SARS-CoV-2 was cloned upstream of an enterokinase
233 cleavage site and a human FC. This plasmid was used to transiently transfect FreeStyle 293F
234 cells using the FreeStyle MAX reagent. The RBD-FC fusion was purified from filtered
235 supernatant on Protein G Sepharose (GE Healthcare). The protein was cleaved using bovine
236 enterokinase (GenScript) leaving a FLAG-tag at the C-terminus of the RBD. Enzyme and FC-
237 portion was removed on HIS-Pur Ni-NTA resin (Thermo Fisher Scientific) and Protein G
238 sepharose (GE Healthcare) respectively, and the RBD was purified by size-exclusion
239 chromatography on a Superdex 200 in 50 mM Tris pH 8, 200 mM NaCl.

240 In addition, the RBD domain (RVQ – VNF) was cloned upstream of a Sortase A recognition site
241 (LPETG) and a 6xHIS tag, and expressed in 293F cells as described above. RBD-HIS was
242 purified from filtered supernatant on His-Pur Ni-NTA resin, followed by size-exclusion
243 chromatography on a Superdex 200.

244 The nanobodies were cloned for expression in the pHEN plasmid with a C-terminal Sortase
245 recognition site (LPETG) and a 6xHIS tag. This plasmid was used to transform BL21 cells for
246 periplasmic expression. Expression was induced with 1 mM IPTG at OD600 = 0.6; cells were
247 grown overnight at 30°C. Nanobodies were retrieved from the periplasm by osmotic shock and
248 purified by Ni-NTA affinity purification and size-exclusion chromatography.

249 Biotinylated and fluorescent probes were generated using Sortase A as described here [16] and
250 here [17]. In brief, nanobodies were site-specifically biotinylated on the C-terminus using
251 Sortase A 5M. Nanobody at a concentration of 50 μM was incubated with sortase A 5M (5 μM),

252 GGGK-biotin (200 μM) in 50 mM Tris, pH 7.5, 150 mM NaCl, 10 mM $CaCl_2$, for 2 hours at 25°C.
253 Unreacted nanobody and sortase was removed with Ni-NTA resin and excess GGGK-biotin was
254 removed with Zeba spin desalting columns (0.5 mL, 7k MWCO, Thermo Fisher Scientific).

255 To generate the fluorescently labeled probes, first a dibenzocyclooctyne-amine (DBCO-amine,
256 Sigma Aldrich) was attached via sortase A to the nanobody or the RBD. (Reaction conditions:
257 50 μM RBD or nanobody, 50 μM Sortase A 5M, 8 mM DBCO-amine in 50 mM Tris pH 7.5, 150
258 mM NaCl, 10 mM $CaCl_2$, 2 hours, 25°C). Unreacted probe, sortase and excess DBCO-amine
259 was removed using Ni-NTA resin and PD-10 columns (GE Healthcare) respectively. Abberior
260 Star 635P-azide (Abberior GMBH) was attached to the DBCO-labeled proteins in a copper-free
261 click chemistry reaction. Unreacted fluorophore was removed on PD-10 column (RBD) or size-
262 exclusion chromatography (nanobody).

263 **Alpaca immunization**

264 Alpaca immunization and phage display was performed similarly as described here [18] and
265 here [19]. In brief, the adult male alpaca Tyson at PreClinics, Germany, was immunized 4 times
266 in a 60-day immunization schedule. SARS-CoV-2 S1-sheep-FC (Native Antigen Company,
267 SKU: REC31806) was used for the first two immunization, and SARS-CoV-2 RBD produced in
268 FreeStyle 293F cells was used for the last two immunizations.

269 **Library generation and nanobody isolation**

270 After the final boost, RNA was isolated from PBMCs (RNA Plus mini kit, Qiagen). For cDNA
271 synthesis, SuperScript III RT (Thermo Fisher Scientific) was used with a combination of
272 oligo(dT), random hexamers, or gene specific primers (AL.CH2,
273 ATGGAGAGGACGTCCTTGGGT and AL.CH2.2 TTCGGGGGGAAGAYRAAGAC) [19].

274 Nanobody sequences were PCR amplified and cloned into a phagemid vector for expression as
275 pIII fusion. This library was electroporated into TG1 cells (Lucigen).

276 Cells were inoculated with VCSM13 helper phage, and the resulting phage was enriched in two
277 consecutive rounds of phage display on RBD immobilized on magnetic beads. After the second
278 round of phage display, individual bacterial colonies were picked in a 96 well format, grown until
279 OD = 0.6 and nanobody expression was induced by addition of 1 mM IPTG. After 16 hours
280 incubation at 30°C, bacterial supernatant was used as primary detection reagent in an ELISA
281 coated with RBD or S ectodomain. Bound nanobodies were detected with anti-E tag (Bethyl
282 laboratories) secondary antibody. Positive clones were sequenced and cloned into the pHEN
283 expression vector for further characterization.

284 **Amino acid sequence of Ty1**

285 MAQVQLVETGGGLVQPGGSLRLSCAASGFTFSSVYMNWVRQAPGKGPEWVSRISPNSGNIG
286 YTDSVKGRFTISRDNAKNTLYLQMNNLKPEDTALYYCAIGLNLSSSSVRGQGTQVTVSS

287 **Next generation sequencing (NGS) and analysis of nanobody libraries.**

288 Plasmids from nanobody libraries before enrichment, and after each enrichment step, were
289 amplified for 13 cycles using Q5 High-Fidelity 2X Master Mix (NEB) according to manufacturer's
290 instructions, using primers:
291 CACTCTTTCCCTACACGACGCTCTTCCGATCTCTCGCGGCCCAGCCGGCCATGG and
292 GGAGTTCAGACGTGTGCTCTTCCGATCTACCGGCGCACCACTAGTGCA, annealing at 72°C.
293 Illumina indexing primers were added using an additional 9 cycles, with Kapa HiFi. Amplicons
294 were size selected using Agencourt AMPure XP beads (bead ratio: 1:1), and were pooled at
295 ratios of 6:2:1 for pre:post-1:post-2 libraries, to account for the reduction in diversity expected

296 during enrichment, and sequenced on an Illumina MiSeq using the MiSeq Reagent Kit v3
297 (2x300) MS-102-3003.

298 Paired-end reads were merged using USEARCH11 [20], and then processed in the Julia
299 language, primarily using the NextGenSeqUtils.jl package [21]. Briefly, reads are trimmed of
300 primer sequences, and deduplicated, maintaining read frequencies. Variant frequencies are
301 calculated as combined frequency of any reads matching a variant within 3% nucleotide
302 divergence, using a kmer-based distance approximation for rapid database search. Any reads
303 with counts >3 from the second enrichment library are searched for their variant frequencies
304 across all databases. When calculating enrichment, to avoid zeros due to sampling and to
305 regularize against over-sensitivity to low-frequency baseline variants, all frequencies are
306 increased by the reciprocal of the size of the pre-enrichment database.

307 **Neutralization Assay**

308 Pseudotyped viruses were generated by the co-transfection of HEK293T cells with plasmids
309 encoding the SARS-CoV-2 spike protein harboring an 18 amino acid truncation of the
310 cytoplasmic tail [22], a plasmid encoding firefly luciferase, and a lentiviral packaging plasmid
311 (Addgene cat#8455) using Lipofectamine 3000 (Invitrogen). Media was changed 12-16 hours
312 after transfection, and pseudotyped viruses were harvested at 48- and 72-hours post
313 transfection, filtered through a 0.45 μm filter, and stored at -80°C until use. Pseudotyped
314 neutralization assays were adapted from protocols previously validated to characterize the
315 neutralization of HIV [23], but with the use of HEK293T-ACE2 cells. Briefly, pseudotyped viruses
316 sufficient to generate ~100,000 RLUs were incubated with serial dilutions of nanobodies for 60
317 min at 37°C. Approximately 15,000 HEK293T-ACE2 cells were then added to each well and the
318 plates were incubated at 37°C for 48 hours. Luminescence was then measured using Bright-Glo

319 (Promega) per the manufacturer's instructions on a GM-2000 luminometer (Promega) with an
320 integration time of 0.3s.

321 **Flow Cytometry**

322 Cells were trypsinized and fixed in 4% formaldehyde/PBS and stained with RBD-AS635P under
323 non-permeabilizing conditions or with Ty1-AS635P under permeabilizing conditions.
324 Fluorescence was quantified using a BD FACSCelesta and the FlowJo software package.

325 **Immunofluorescence**

326 Vero E6 cells were seeded onto coverslips in a 24 well plate and incubated overnight at
327 37°C/5% CO_2. Cells were infected with SARS-CoV-2 at a MOI of 1 for 24 h. Cells were fixed
328 with 4% (v/v) formaldehyde, permeabilized in 0.5% Triton X-100 and blocked in 5% horse
329 serum. Cells were incubated with anti-dsRNA antibody (1:2000, J2 Scicons) for 1 hour at room
330 temperature followed by 1 hour staining with the secondary antibody anti-mouse-Alexa488
331 (1:2000, Thermo Fisher Scientific), Hoechst (1:1000, Invitrogen) and Ty1-AS635P (0.05 µg/mL).
332 Coverslips were mounted in mounting media and images were obtained using Zeiss Axiovert
333 microscope and processed using Adobe Photoshop.

334 **Biolayer interferometry (BLI)**

335 BLI was performed using single-use high-precision streptavidin biosensors (SAX) on an eight-
336 channel Octet RED instrument according to manufacturer's protocols (Fortebio)[24]. Assays
337 were performed in 2xPBS comprising 0,05% Tween-20 (PBST). Biotinylated nanobodies Ty1
338 and NP-VHH1 were loaded at concentrations between 30 and 250 nM followed by quenching
339 using biocytin to reach final sensor loads of between 0.15 and 0.7 nm.

340 For the comparative binding test, the eight sensors were divided into two sets, each comprising
341 double sample as well as single reference and single control sensors. Sample and reference
342 sensors were loaded with respective nanobodies. The SAX control was only quenched. Loading
343 of the two sets was performed consecutively to reach similar immobilization levels, while
344 subsequent association and dissociation phases were performed simultaneously. For
345 association, the sample and control sensors were dipped into RBD, while the reference sensor
346 was dipped into PBST. For titration experiments, all sensors were loaded simultaneously.
347 During association one of the sensors was used as reference and only dipped into PBST.

348 Raw data were pre-processed, analyzed and fitted by applying the 1:1 binding model as
349 implemented in the manufacturer's software[25] . The processed data were imported into
350 Rstudio for visualization and further analysis [26–28]. The comparative binding test shown in
351 Figure 3A comprises un-processed raw data. The titration data in Figure 3B were processed
352 applying reference sensor subtraction and Savitzky-Golay filter operations. Raw data and the
353 analysis visualization scripts will be uploaded to Dryad and/or Github.

354 **Cryo-EM sample preparation and imaging**

355 Spike trimer (0.7 mg/ml) and Ty1 (1.3 mg/ml) were mixed in a 1:8 molar ratio and incubated on
356 ice for 5 minutes. A 3-µl aliquot of the sample solution was applied to glow-discharged CryoMatrix
357 holey grids with amorphous alloy film (Zhenjiang Lehua Technology) in a Vitrobot Mk IV (Thermo
358 Fisher Scientific) at 4 degrees and 100% humidity (blot 10 s, blot force 3).
359 Cryo-EM data collection was performed with EPU 2.7 (Thermo Fisher Scientific) using a Krios G3i
360 transmission-electron microscope (Thermo Fisher Scientific) operated at 300 keV in the
361 Karolinska Institutet 3D-EM facility. Images were acquired in nanoprobe EFTEM mode with a slit
362 width of 10 eV using a GIF 967 energy filter (Ametek) and a K3 detector (Ametek) during 2.4
363 seconds with a dose rate of 4.1 e-/px/s resulting in a total dose of 38 $e^-/Å^2$ fractionated into 40

364 movie frames. Motion correction, CTF-estimation, fourier binning (to 1.02 Å/px), picking and
365 extraction were performed on the fly using Warp [29].
366 A total of 9,584 micrographs were and 350,022 particles were picked by Warp. Extracted particles
367 were imported into cryoSPARC v2.15.0 [30] for 2D classification, 3D classification and non-
368 uniform 3D refinement. The particles were processed with C1 symmetry throughout. After 2D
369 classification (300 classes) 219,491 particles were retained and used to build three ab-initio 3D
370 reconstructions. These were further processed for heterogenous refinement that resulted in one
371 reconstruction showing high-resolution structural features in the core of the spike. One round of
372 homogenous refinement followed by non-uniform refinement resulted in a final reconstruction to
373 an overall resolution of 2.9 Å (0.143 FSC) using 150,847 particles.
374
375 **Model building and structure refinement**
376 A structure of the 2019-nCoV spike protein trimer [14] (PDB: 6VSB) was used as a starting model
377 for model building. The model was extended and manually adjusted in COOT [31]. The Nanobody
378 structure was homology modelled using SWISS-MODEL [32] taking PDB:5JMR [33] as a
379 template. The missing regions of the RBD domains were built based on the RBD-Spike crystal
380 structure (PDB: 6LZG) [34]. Structure refinement and manual model building were performed
381 using COOT and PHENIX [35] in interspersed cycles with secondary structure and geometry
382 restrained. All structure figures and all EM density-map figures were generated with UCSF
383 ChimeraX [36].
384
385
386 **Acknowledgements**
387 SARS-CoV-2 virus was received from Jonas Klingström, KI. The authors thank James Voss
388 and Deli Huang for reagents. We thank PreClinics for their fast and efficient services and
389 Gunnar Schulte and Per-Åke Nygren for providing access to instruments for measuring binding

390 kinetics. We also thank Fondation Dormeur, Vaduz for generous support of flow cytometry
391 equipment.This work was supported by an EU grant (CoroNAb) to BM, GM and GHK and by
392 project grants from the Swedish Research Council to BM (2018-02381), BMH (2017-6702 and
393 2018-3808) and to GM (2018-03843).
394
395 The authors declare no conflict of interest
396
397 **Bibliography**

398 1. Shang J, Wan Y, Luo C, Ye G, Geng Q, Auerbach A, et al. Cell entry mechanisms of
399 SARS-CoV-2. Proc Natl Acad Sci U S A. 2020;117: 11727–11734.

400 2. Wrapp D, Wang N, Corbett KS, Goldsmith JA, Hsieh C-L, Abiona O, et al. Cryo-EM
401 structure of the 2019-nCoV spike in the prefusion conformation. Science. 2020;367: 1260–
402 1263.

403 3. Walls AC, Park Y-J, Tortorici MA, Wall A, McGuire AT, Veesler D. Structure, Function, and
404 Antigenicity of the SARS-CoV-2 Spike Glycoprotein. Cell. 2020;181: 281–292.e6.

405 4. Ju B, Zhang Q, Ge J, Wang R, Sun J, Ge X, et al. Human neutralizing antibodies elicited by
406 SARS-CoV-2 infection. Nature. 2020. doi:10.1038/s41586-020-2380-z

407 5. Shi R, Shan C, Duan X, Chen Z, Liu P, Song J, et al. A human neutralizing antibody targets
408 the receptor binding site of SARS-CoV-2. Nature. 2020. doi:10.1038/s41586-020-2381-y

409 6. Cao Y, Su B, Guo X, Sun W, Deng Y, Bao L, et al. Potent neutralizing antibodies against
410 SARS-CoV-2 identified by high-throughput single-cell sequencing of convalescent patients'
411 B cells. Cell. 2020. doi:10.1016/j.cell.2020.05.025

412 7. Bannas P, Hambach J, Koch-Nolte F. Nanobodies and Nanobody-Based Human Heavy

413 Chain Antibodies As Antitumor Therapeutics. Front Immunol. 2017;8: 1603.

414 8. Vincke C, Loris R, Saerens D, Martinez-Rodriguez S, Muyldermans S, Conrath K. General
415 strategy to humanize a camelid single-domain antibody and identification of a universal
416 humanized nanobody scaffold. J Biol Chem. 2009;284: 3273–3284.

417 9. Detalle L, Stohr T, Palomo C, Piedra PA, Gilbert BE, Mas V, et al. Generation and
418 Characterization of ALX-0171, a Potent Novel Therapeutic Nanobody for the Treatment of
419 Respiratory Syncytial Virus Infection. Antimicrob Agents Chemother. 2016;60: 6–13.

420 10. Cardoso FM, Ibañez LI, Van den Hoecke S, De Baets S, Smet A, Roose K, et al. Single-
421 domain antibodies targeting neuraminidase protect against an H5N1 influenza virus
422 challenge. J Virol. 2014;88: 8278–8296.

423 11. Hanke L, Knockenhauer KE, Brewer RC, van Diest E, Schmidt FI, Schwartz TU, et al. The
424 Antiviral Mechanism of an Influenza A Virus Nucleoprotein-Specific Single-Domain
425 Antibody Fragment. MBio. 2016;7. doi:10.1128/mBio.01569-16

426 12. Kirchhofer A, Helma J, Schmidthals K, Frauer C, Cui S, Karcher A, et al. Modulation of
427 protein properties in living cells using nanobodies. Nat Struct Mol Biol. 2010;17: 133–138.

428 13. Pollard TD. A guide to simple and informative binding assays. Mol Biol Cell. 2010;21:
429 4061–4067.

430 14. Wrapp D, De Vlieger D, Corbett KS, Torres GM, Wang N, Van Breedam W, et al. Structural
431 Basis for Potent Neutralization of Betacoronaviruses by Single-Domain Camelid Antibodies.
432 Cell. 2020;181: 1004–1015.e15.

433 15. Monteil V, Kwon H, Prado P, Hagelkrüys A, Wimmer RA, Stahl M, et al. Inhibition of SARS-
434 CoV-2 Infections in Engineered Human Tissues Using Clinical-Grade Soluble Human

435 ACE2. Cell. 2020;181: 905–913.e7.

436 16. Antos JM, Ingram J, Fang T, Pishesha N, Truttmann MC, Ploegh HL. Site-Specific Protein
437 Labeling via Sortase-Mediated Transpeptidation. Curr Protoc Protein Sci. 2017;89: 15.3.1–
438 15.3.19.

439 17. Witte MD, Theile CS, Wu T, Guimaraes CP, Blom AEM, Ploegh HL. Production of
440 unnaturally linked chimeric proteins using a combination of sortase-catalyzed
441 transpeptidation and click chemistry. Nat Protoc. 2013;8: 1808–1819.

442 18. Sosa BA, Demircioglu FE, Chen JZ, Ingram J, Ploegh HL, Schwartz TU. How lamina-
443 associated polypeptide 1 (LAP1) activates Torsin. Elife. 2014;3: e03239.

444 19. Alpaca (Lama pacos) as a convenient source of recombinant camelid heavy chain
445 antibodies (VHHs). J Immunol Methods. 2007;324: 13–25.

446 20. Edgar RC, Flyvbjerg H. Error filtering, pair assembly and error correction for next-
447 generation sequencing reads. Bioinformatics. 2015;31: 3476–3482.

448 21. Kumar V, Vollbrecht T, Chernyshev M, Mohan S, Hanst B, Bavafa N, et al. Long-read
449 amplicon denoising. Nucleic Acids Res. 2019;47: e104.

450 22. Rogers TF, Zhao F, Huang D, Beutler N, Burns A, He W-T, et al. Rapid isolation of potent
451 SARS-CoV-2 neutralizing antibodies and protection in a small animal model. bioRxiv. 2020.
452 p. 2020.05.11.088674. doi:10.1101/2020.05.11.088674

453 23. Sarzotti-Kelsoe M, Bailer RT, Turk E, Lin C-L, Bilska M, Greene KM, et al. Optimization and
454 validation of the TZM-bl assay for standardized assessments of neutralizing antibodies
455 against HIV-1. J Immunol Methods. 2014;409: 131–146.

456 24. Abdiche Y, Malashock D, Pinkerton A, Pons J. Determining kinetics and affinities of protein

457 interactions using a parallel real-time label-free biosensor, the Octet. Anal Biochem.
458 2008;377: 209–217.

459 25. Octet Systems Software \textbar ForteBio. Available:
460 https://www.fortebio.com/products/octet-systems-software

461 26. Wickham H. ggplot2: Elegant Graphics for Data Analysis. Springer; 2016.

462 27. Wickham H. tidyverse: Easily Install and Load the 'Tidyverse. R package version 1.2.1;
463 2017. Available: http://CRAN.R-project.org/package=tidyverse

464 28. Team RC. R: A language and environment for statistical computing. Vienna, Austria: R
465 Foundation for Statistical Computing; Available: http://www.R-project.org/

466 29. Tegunov D, Cramer P. Real-time cryo-electron microscopy data preprocessing with Warp.
467 Nat Methods. 2019;16: 1146–1152.

468 30. Punjani A, Rubinstein JL, Fleet DJ, Brubaker MA. cryoSPARC: algorithms for rapid
469 unsupervised cryo-EM structure determination. Nat Methods. 2017;14: 290–296.

470 31. Emsley P, Lohkamp B, Scott WG, Cowtan K. Features and development of Coot. Acta
471 Crystallogr D Biol Crystallogr. 2010;66: 486–501.

472 32. Waterhouse A, Bertoni M, Bienert S, Studer G, Tauriello G, Gumienny R, et al. SWISS-
473 MODEL: homology modelling of protein structures and complexes. Nucleic Acids Res.
474 2018;46: W296–W303.

475 33. Dahms SO, Creemers JWM, Schaub Y, Bourenkov GP, Zögg T, Brandstetter H, et al. The
476 structure of a furin-antibody complex explains non-competitive inhibition by steric exclusion
477 of substrate conformers. Sci Rep. 2016;6: 34303.

478 34. Wang Q, Zhang Y, Wu L, Niu S, Song C, Zhang Z, et al. Structural and Functional Basis of
479 SARS-CoV-2 Entry by Using Human ACE2. Cell. 2020;181: 894–904.e9.

480 35. Adams PD, Afonine PV, Bunkóczi G, Chen VB, Davis IW, Echols N, et al. PHENIX: a
481 comprehensive Python-based system for macromolecular structure solution. Acta
482 Crystallogr D Biol Crystallogr. 2010;66: 213–221.

483 36. Goddard TD, Huang CC, Meng EC, Pettersen EF, Couch GS, Morris JH, et al. UCSF
484 ChimeraX: Meeting modern challenges in visualization and analysis. Protein Sci. 2018;27:
485 14–25.

486 37. Myszka DG, Jonsen MD, Graves BJ. Equilibrium analysis of high affinity interactions using
487 BIACORE. Anal Biochem. 1998;265: 326–330.

488

489

490

491

492

493

494

495

496

497

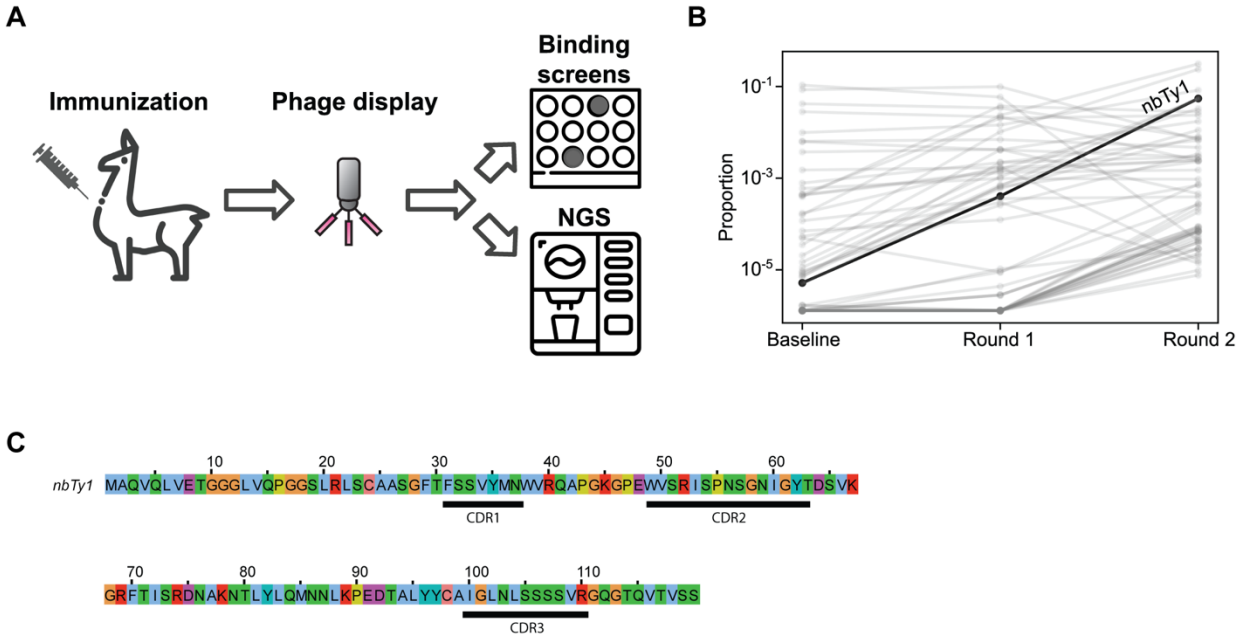

Figure 1 - Nanobody discovery.

A - Overview of nanobody generation process.

B - Variant frequencies quantified by NGS across successive enrichment steps. Identified using RBD bait, Ty1 exhibits the greatest total fold change of all nanobodies, increasing in proportion over 10,000-fold between initial and final libraries.

C - Sequence of Ty1. Complementarity-determining regions (CDRs) are indicated. Color scheme according to ClustalX.

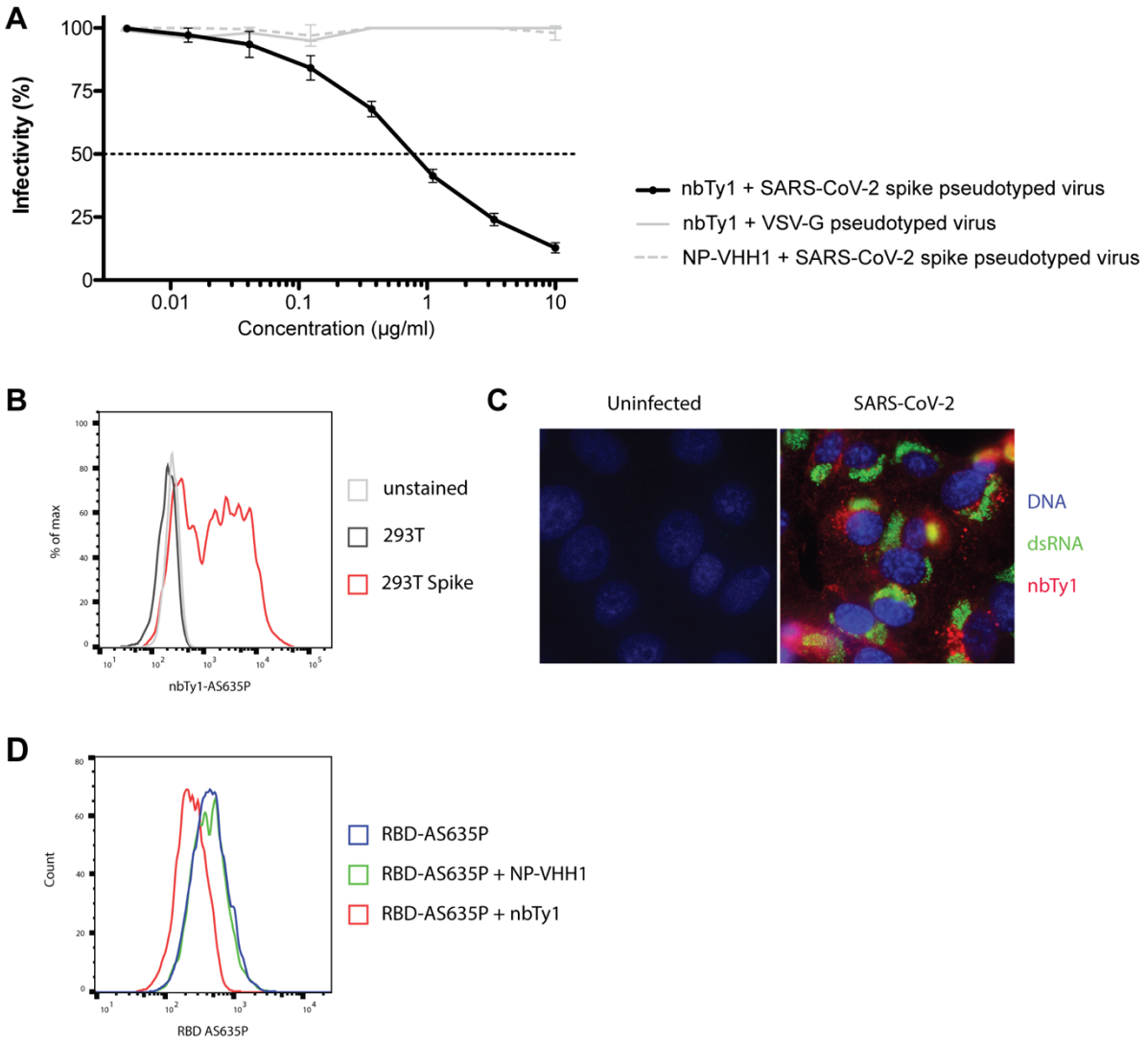

Figure 2 - Nanobody Ty1 neutralizes SARS-CoV-2 and specifically recognizes SARS-CoV-2 spike glycoprotein.

A - VSV G or SARS-CoV-2 spike pseudotyped lentivirus was incubated with a dilution series of Ty1 or control nanobody (influenza NP-VHH1 [11]). Infectivity relative to cells infected with pseudotyped virus in the absence of nanobody is shown. Neutralization by Ty1 was repeated in duplicate across 6 assays, and the error bars represent the standard deviation.

B - Cells were transfected with a plasmid harboring the SARS-CoV-2 spike for 24 h. Cells were fixed, permeabilized and stained with Ty1-AS635P (black and red) or left unstained (grey). Cells were analyzed by flow cytometry. Cell counts are presented as % of max (representative

histogram).

C - Vero E6 cells were infected with SARS-CoV-2 at a MOI of 1 for 24 hours. Cells were fixed, permeabilized and stained for DNA (blue), dsRNA (green) and with Ty1-AS635P (red). Pictures were taken by fluorescence microscopy and representative examples are shown.

D - ACE2 expression 293T cells were trypsinized, fixed and stained with RBD-AS635P alone, or preincubated with IAV NP-VHH1 or Ty1. Cells were analyzed by flow cytometry.

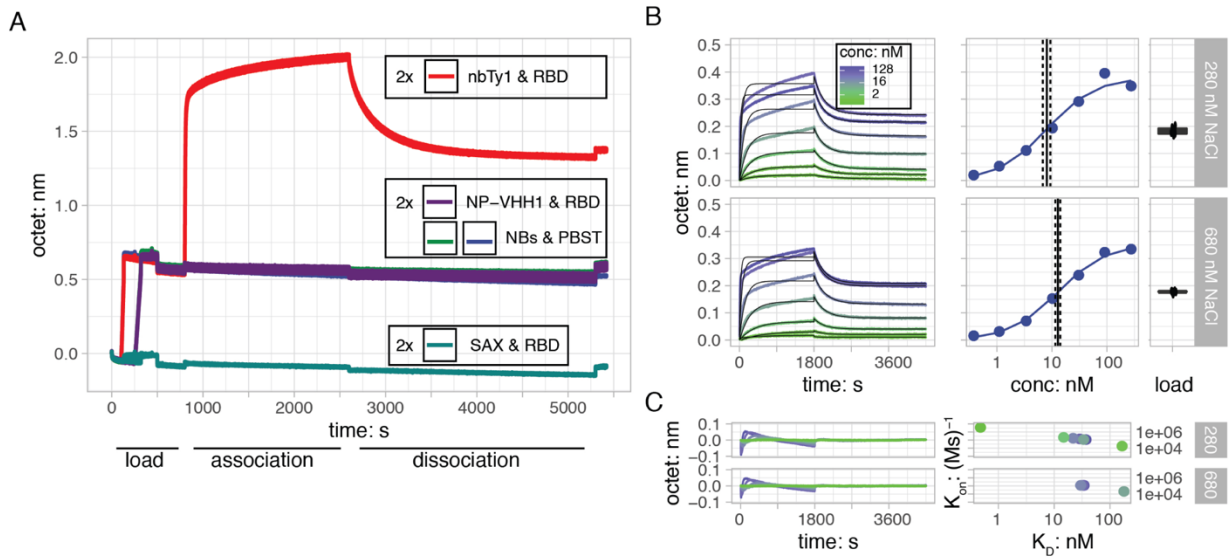

Figure 3 - RBD bound to surface-immobilized Ty1 with high affinity in the 5-50 nM range in Biolayer Interferometry

A - RBD bound to surface-immobilized Ty1 (red curves), but not to NP-VHH1 (violet curves) or to biocytin-quenched Streptavidin (SAX, green curves). Almost equal nanobody immobilization levels of about 0.7 nm were obtained by first loading Ty1 and then NP-VHH1. The SAX control surface (green) was quenched, but not loaded with nanobodies. During association, nanobody sample and control SAX sensors (red, violet and green) were dipped into RBD, while the reference nanobody sensors were dipped into PBST (blue and light-green). For dissociation, all sensors

543 were dipped into PBST. Binding of molecules over time is recorded as sensorgrams recording
544 the shift in wavelengths (unit: nm) due to an increase in the optical thickness of the surface layer.
545 B - *(left)* RBD titration sensorgrams reveal concentration-dependent responses with an
546 association phase comprising a fast and a slow component. Dissociation seems to follow a single-
547 exponential decay but does not return to baseline over the measurement time. Fitted 1:1 binding
548 models are shown as thin lines. *(middle)* Pseudo-equilibrium response values extracted from the
549 final association phase were plotted against the logarithmic Ty1 concentration. Single-site
550 interaction fits of the sigmoidal binding curves according to [37] yielded K_D-values in the low nM
551 range. K_D-values and standard deviations are shown as solid and dotted lines, respectively. *(right)*
552 Sensor immobilization levels are shown as jittered box plots.
553 C - *(left)* Residuals of the 1:1 model fits to the interaction sensorgrams revealed that the simple
554 1:1 interaction model did not fully explain the obtained data, especially association phases at
555 higher RBD concentrations. Color coding as in the sensorgram above. *(right)* Plot of fitted
556 association rate constants (kon) versus affinity (K_D) values obtained from the kinetic 1:1 fits. Most
557 of the fits grouped together at K_D values of 10-100 nM with association and dissociation constants
558 of about 1-1.2 $*10^5$ $(Ms)^{-1}$ and 3.5–4.3$*10^{-3}$ s^{-1}, respectively.
559

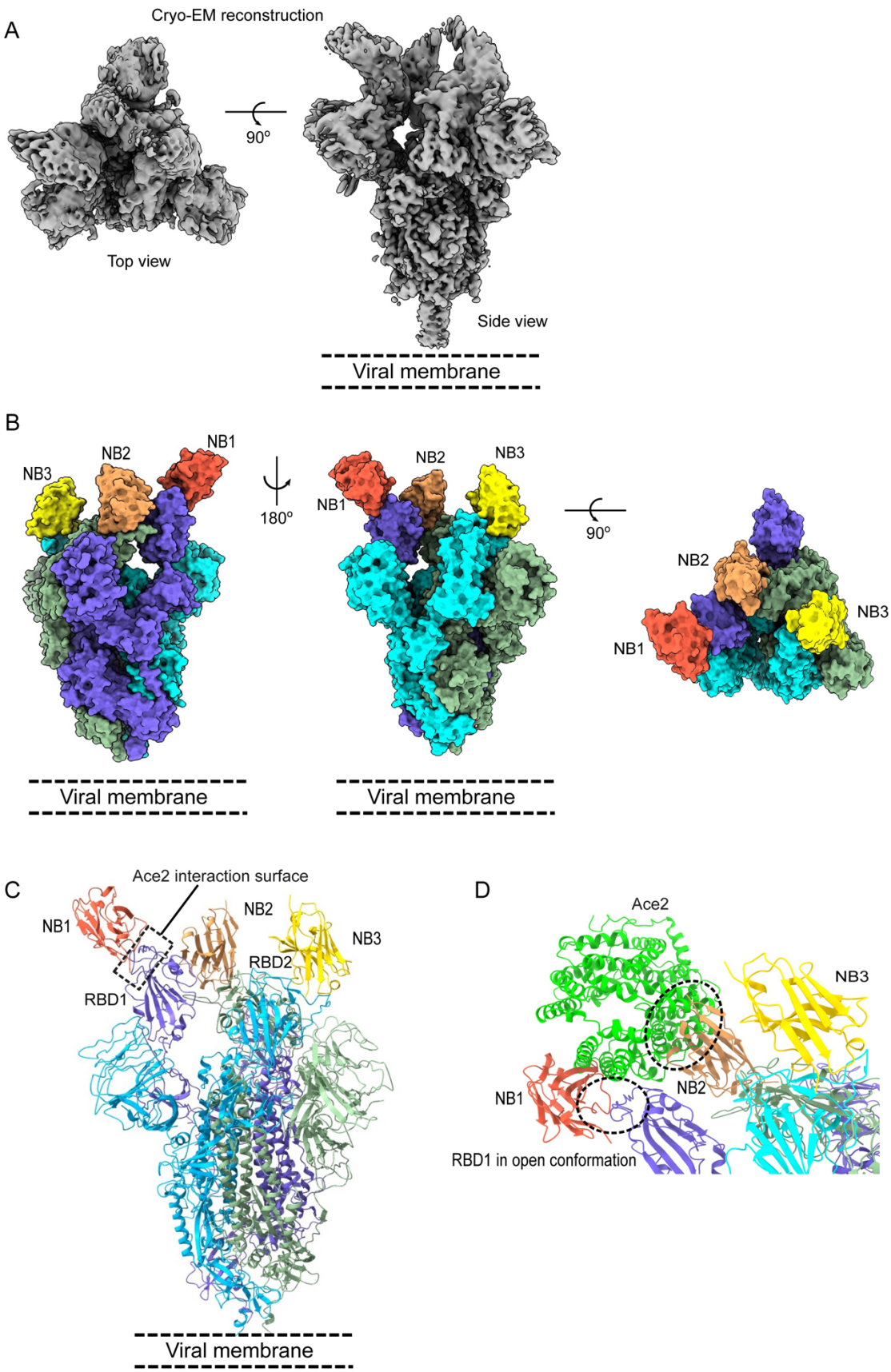
A
Cryo-EM reconstruction
90°
Top view
Side view
Viral membrane
B
NB1
NB2
NB3
180°
90°
Viral membrane
Viral membrane
C
Ace2 interaction surface
NB1
NB2
NB3
RBD2
RBD1
Viral membrane
D
Ace2
NB3
NB1
NB2
RBD1 in open conformation

560

561 **Figure 4 - Structure of the SARS-CoV-2 spike in perfusion conformation in complex with**
562 **neutralizing nanobody Ty1**
563
564 **Ty1 binds to the RBD in ‘up’ and ‘down’ conformation and prevents ACE2 engagement**
565
566 A - Cryo-EM reconstruction to an overall resolution of 2.9 Å of the spike trimer with bound Ty1
567 B - Surface representation of the spike trimer with three molecules of Ty1 bound. In our
568 reconstruction, one RBD takes the ‘up’ and two RBDs have the ‘down’ conformation. Ty1 is
569 bound on all three RBDs.
570 D - Cartoon representation of the spike trimer in complex with three molecules of Ty1.
571 E - Ty1 shows a two-pronged inhibition of ACE2 receptor binding through binding the RBD in
572 the ‘up’ conformation and by binding to the neighboring RBD in the ‘down’ conformation.